J Adv Ceram

Research Article

High-strength anisotropic ZrC/YSZ composite foams achieved by *in situ* carbothermal reduction of ice-templated YSZ foams

Xiaohui Fan[1,✉], Qianyu Yao[2], Na Ni[3,✉], Xin Wang[4], Kolan Madhav Reddy[1], Fangwei Guo[1], Xiaofeng Zhao[1]

Cite this article: Fan X, Yao Q, Ni N, et al. *J Adv Ceram* 2026, **15**(3): 9221247. https://doi.org/10.26599/JAC.2026.9221247

ABSTRACT: Achieving high strength in porous zirconium carbide (ZrC)-based ceramics is notoriously challenging, primarily due to their high inherent porosity. Here, we present a creative, *in situ* synthesis strategy that utilizes anisotropic 3 mol% yttria-stabilized zirconia (YSZ) ice-templated foam as a reactive template. This novel approach yields a ZrC/YSZ composite foam with a high average axial compressive strength of 61.5 MPa at a porosity of ~70.9% at room temperature. The ZrC phase nucleates and grows for the first time within dense YSZ struts, not just on the surface. This unique reaction is intimately linked to the redistribution of Y^{3+} ions and the consequent tetragonal (t) to cubic (c) phase transformation in the YSZ matrix. Phase transformation in the matrix is a critical internal lever governing the mechanical properties, in some cases exceeding the influence of geometric factors. This research not only offers a new route to fabricate high-strength ultrahigh-temperature ceramic composite foams but also unveils the intricate interplay between their internal reaction chemistry and macroscopic mechanical strength.

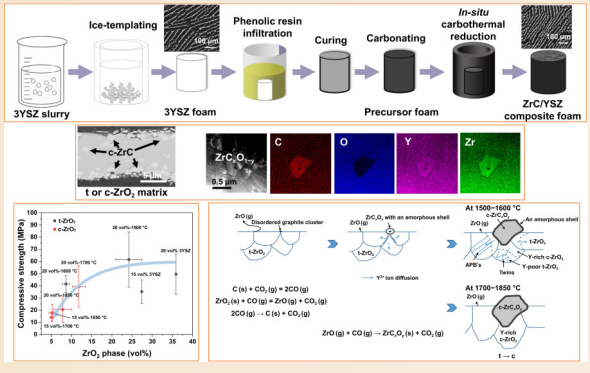

KEYWORDS: zirconium carbide (ZrC); ice templating; foam; mechanical properties

1 Introduction

Zirconium carbide (ZrC) is an important member of ultrahigh temperature ceramics (UHTCs), as it has a melting temperature of ~3500 °C, low density (6.6 g/cm^3) and high thermal conductivity (20–40 W/(m·K)). Its high hardness (~25 GPa), elastic modulus (~400 GPa), and excellent property retention at high temperature make ZrC the most promising candidate material in "hot zone" parts of hypersonic vehicles, such as leading edges, combustors, and thermal protection systems [1]. Meanwhile, ZrC-based porous ceramics, coupled with transpiration cooling systems [2] and insulation packages [3], have the potential to extend the service life of hypersonic vehicles. They are also attractive in gas absorption or filtration at temperatures over 2000 °C.

ZrC-based porous ceramics are widely prepared via partial sintering [4,5], evaporating solvent and hot pressing [6], sol–gel [7,8], direct foaming [9,10], melt infiltration [11], molten salt-assisted template methods [12], etc. These ceramics featuring randomly distributed spherical pores and well-oriented directional pores have been developed by direct hole-making and sacrificial templates, respectively. With regard to porous ceramics, the pore characteristics are key to their strength [13]. Well-oriented channels provide excellent permeability together with high mechanical strength [14]. The facile techniques, including freeze-casting [15] and templating [11], can guide the preparation of ceramics with highly anisotropic aligned pores, which exhibit high compressive strength in specific loading directions. However, due to the difficulty of sintering, pores in the cellular walls of UHTC may decrease the strength when freeze-casting aqueous UHTC-based suspensions [15]. By using carbon sacrificial templates, e.g., biocarbon [16] and carbon foam [11], a low volume fraction of ZrC was obtained, and a carbon strut was retained in the ZrC/C porous ceramics. Dense and continuous ZrC on the strut of the porous composite ceramic was hardly achieved; therefore, the strength decreased from 31.25 to 0.3 MPa as the porosity increased from 55% to 85% when prepared through the above methods, as shown in Table 1. It is true that a high-entropy strategy can help improve the compressive strength. For example, a $(Ta_{0.2}Nb_{0.2}Ti_{0.2}Zr_{0.2}Hf_{0.2})C$ sample with a porosity of 91.3% [10] shows a high compressive strength of 28.1 MPa. However, most of the compressive strengths were lower than 6 MPa, especially when the porosity increased to 70%.

[1] Shanghai Key Laboratory of Advanced High Temperature Materials and Precision Forming, School of Materials Science and Engineering, Shanghai Jiao Tong University, Shanghai 200240, China. [2] Huawei Technologies Co., Ltd., Shenzhen 518129, China. [3] Key Lab of Education Ministry for Power Machinery and Engineering, School of Mechanical Engineering, Shanghai Jiao Tong University, Shanghai 200240, China. [4] Wiseyear Technology Co., Ltd., Haining 314400, China.

✉ Corresponding authors. E-mail: X. Fan, xhfan@sjtu.edu.cn; N. Ni, na.ni@sjtu.edu.cn

Received: August 21, 2025; Revised: December 19, 2025; Accepted: January 11, 2026

Table 1 Porosity and compressive strength of ZrC-based ceramic foams prepared by different methods

Material	Preparation method	Porosity (%)	Compressive strength (MPa)	Ref.
ZrC	Partially sintering	68.74	8.28	[4]
$(Zr_{0.2}Hf_{0.2}Ti_{0.2}Nb_{0.2}Ta_{0.2})C$	Partially sintering	80.99	3.45	[5]
ZrC	Evaporating solvent and hot-pressing	73.5	5.67	[6]
		67.8	19.6	
		62.2	27.5	
		55.4	31.25	
ZrC	Direct foaming	85	0.4	[9]
$(Ta_{0.2}Nb_{0.2}Ti_{0.2}Zr_{0.2}Hf_{0.2})C$	Self-foaming	91.3	28.1	[10]
ZrC/C	Melt infiltration using carbon foam as template	75.38	26.5	[11]
ZrC/SiC	Sol–gel	80	0.4	[21]
		40	0.67	
ZrC/SiC	Sol–gel	69.8	0.7	[22]
		73.4	0.3	

Zirconia, a widely used structural ceramic, is usually carbothermally reduced to synthesize ZrC. Single crystals of yttria-stabilized zirconia (YSZ) have excellent mechanical properties with a fracture toughness of ~8 $MPa{\cdot}m^{1/2}$ [17]. The compressive strength of YSZ foam with a porosity of 65%–77% was 3–27 MPa [18], and that of ice-templated porous zirconia can be tuned from 5.5 to 28 MPa at a porosity level of ~73% [19]. Moreover, in a previous study [20], yttria-stabilized zirconium dioxide assisted the consolidation of ZrC, enhancing the strength and fracture toughness of ZrC-based composites.

In this study, we proposed using an ice-templated YSZ foam as a template to prepare anisotropic ZrC-based porous ceramic *in situ*, whose compressive strength reached 38.6 MPa under radial loading at a porosity of 72.7%. First, 3 mol% YSZ foams were ice-templated and sintered to obtain the t phase. 3YSZ foam precursors were subsequently infiltrated by phenolic resin. Then, the composite foam precursors were cured and carbonized. The ZrC/YSZ composite foam was finally obtained through a carbothermic reduction process at high temperature. A hybrid structure was observed. The compressive strength of the composite foams was measured, and a schematic of the synthesis of ZrC was discussed.

2 Materials and method

2.1 Raw materials

3 mol% YSZ powder (99% pure, D_{50} = 300 nm, Jiangxi Fanmeiya Materials Co., Ltd., China) was used as the raw material. Ammonium polyacrylate (APA) was used as a dispersant, and polyvinyl alcohol (PVA) was used as a binder. Phenol-formaldehyde resin (Shanghai Macklin Biochemical Technology Co., Ltd., China) was used as the carbon source.

2.2 Foam preparation

As depicted in Fig. 1, 15 and 20 vol% solid loadings of 3YSZ slurry were prepared via a high-energy ball milling (01-HDDM, Qingdao Lianrui Precision Machinery Limited Company, China) according to a previous work [23]. 3YSZ foam was prepared with a diameter of 18 mm and a height of 20 mm at a cooling speed of about −10 °C/min by using a homemade ice-templated setting [24]. Then, the 3YSZ prefoam was sintered at 1300 °C for 2 h in a furnace (SXL-1400C, Shanghai SIOMM Precision Instrument Manufacturing Co., Ltd., China). The purchased phenolic resin (P832682, Macklin, China) was dissolved in ethanol at 80 wt% before vacuum infiltration, which was carried out by a planetary vacuum mixer (SMIDA TMV-200T, Simida Intelligent Equipment Co., Ltd., China) for 3 min at 0.05 Pa. Then, the infiltrated foam and excessive resin were transferred to an alumina crucible before being cured at 110 °C for 5 h. Then, this foam was carbonated in a tube furnace (GSL-1700X, Shenyang Kejing Auto-instrument Co., Ltd., China) at 1100 °C for 2 h in flowing argon. Finally, ZrC/YSZ composite foam was synthesized via *in situ* carbon thermal reduction at 1500, 1600, 1700, and 1850 °C for 2 h in a furnace (hot pressing sintering furnace, Chenhua Ltd., China) in flowing argon. Composite foam samples are named in the way of "volume fraction of solid loading of 3YSZ slurry"—"temperature at which carbon thermal reduction took place". For example, 15 vol%-1700 °C means that the 3YSZ template foam has an initial 15 vol% solid loading of slurry and is carbothermally reduced at 1700 °C.

2.3 Characterization

X-ray diffraction (XRD) patterns were collected from mashed composite foams at a speed of 1° per minute by using an X-ray diffractometer (D8 ADVANCE Da Vinci, Bruker, Germany) with a Cu target (40 kV, 40 mA). The lattice parameter was refined by the Rietveld method. The measured density of the ZrC/YSZ composite foam, ρ_m, was calculated as the mass of the foam divided by its volume. The porosity is estimated by $1 - \rho_m/\rho_t$, where the theoretical density of the ZrC/YSZ composite foam, ρ_t, was estimated by volume fractions of ZrC and YSZ obtained from XRD data and their theoretical densities (ρ_{ZrC} = 6.73 g/cm^3 and ρ_{3YSZ} = 6.05 g/cm^3). The values of ρ_m and ρ_t of the composite foams and 3YSZ foams are listed in Table S1 in the Electronic Supplementary Material (ESM). A two-sample t-test (null hypothesis: no difference in the means) was used to evaluate the differences (significance level: 0.05) in porosity within the 3YSZ template foams and 15 vol% ZrC/YSZ composite foams. A one-way ANOVA (null hypothesis: no difference in the means) was carried out to evaluate the difference (significance level: 0.05) in the 20 vol% ZrC/YSZ group. If the mean difference was significant, Tukey's test was carried out to evaluate it in pairs sequentially. The microstructure of the foams was characterized by a scanning electron microscope (SEM; Mira3 and Rise-magna, Tescan, Czech Republic) and a transmission electron microscope (TEM; JEM-ARM200F, JEOL, Japan). Element mapping was also performed via energy dispersive spectroscopy (EDS). Raman scattering was induced by a 75 nW 532 nm laser equipped with a microscope (Rise-Magna). The light element of C was mapped at

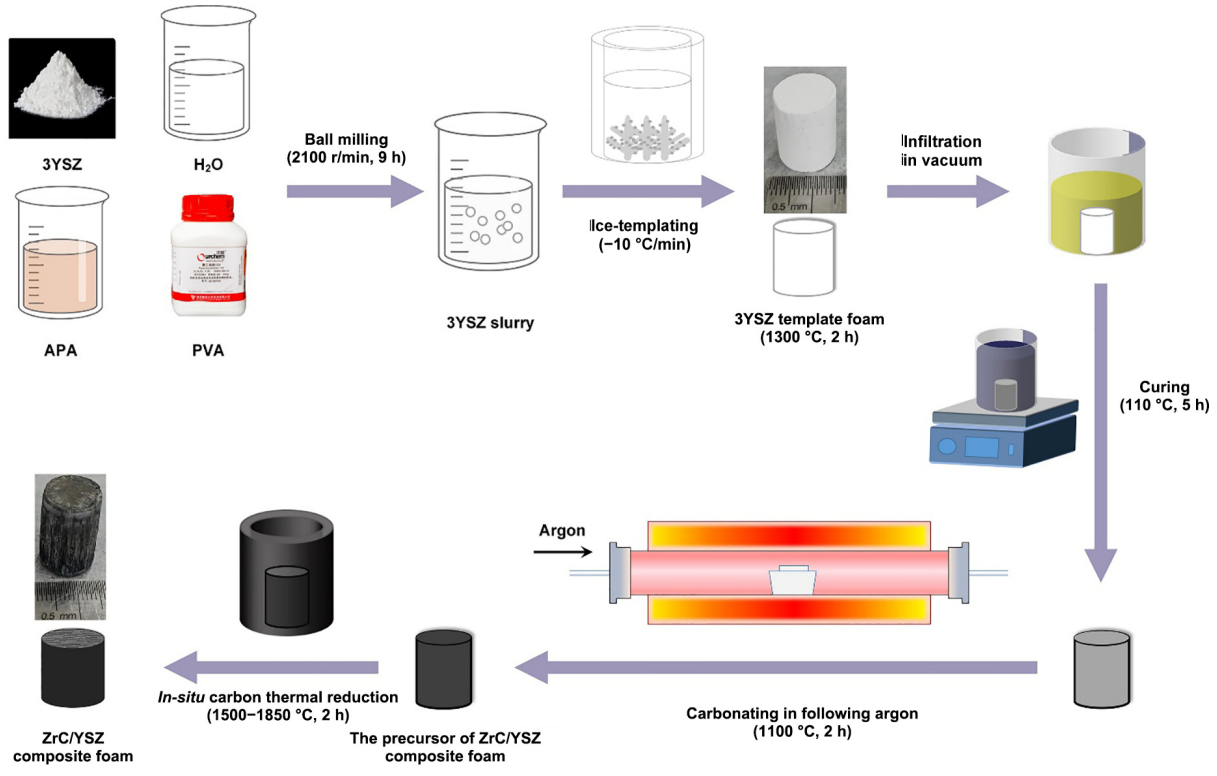

Fig. 1 Schematic diagram of preparation of ZrC/YSZ composite foam.

20 kV by an electron probe microanalyzer (EPMA; JEOL-JXA 8230, JEOL, Japan) along with elements of Zr, Y, and O at room temperature. Compressive strength tests were carried out by using a testing machine (Zwick/Roell Z020, Germany) with a crosshead speed of 0.5 mm/min. Samples for compression tests were cut into 5 mm × 5 mm × 5 mm pieces from a resin-infiltrated ZrC/YSZ composite foam ~15 mm in diameter and ~18 mm in height. Then, the resin in the cut samples was thermally removed at 330 °C for 2 h in a furnace in air with a 1 °C/min heating rate. At least five specimens were prepared for each sample.

3 Results and discussion

3.1 Characterization of the 3YSZ template foam and ZrC/YSZ composite foam

As shown in Fig. 2, the raw material of the 3YSZ powder had mixed m-ZrO_2 and t-ZrO_2 phases, while the m phase was fully transformed to the t phase in ice-templated 3YSZ foam with the t-ZrO_2 phase after sintering at 1300 °C for 2 h. The c-ZrC phase in the ZrC/YSZ composite foam was generated at a starting temperature of 1500 °C, and its content increased as the temperature increased to 1850 °C. Both c-ZrC and t- or c-ZrO_2 were found in ZrC/YSZ composite foams, in which t-ZrO_2 was characterized at 1500 and 1600 °C and c-ZrO_2 at 1700 and 1850 °C. The phase compositions of each sample were obtained by XRD pattern Rietveld refinement in powder of composite foam and are listed in Table 2. Referenced ICDD PDF cards are presented in Table S2 in the ESM, and their reliability is shown in Table S3 and Figs. S1 and S2 in the ESM.

The porosities of the sintered ice-templated 3YSZ foam in the 15 and 20 vol% solid loadings were 75.3%±2.5% and 69.8%±5.0%, respectively. The porosity of composite foams, phase volume fractions (V_f) in powder and in foam and the corresponding lattice parameters were also present. This result indicated that more than 16 vol% of the c-ZrC phase was synthesized at temperatures of 1600 °C and above. A small volume fraction of ~4.4 vol% c-ZrC was carbothermally reduced from t-ZrO_2 at 1500 °C. Residues of YSZ in the struts of the composite foam involved two phases, i.e., the *t* phase at low temperatures (1500 and 1600 °C) and the c phase at high temperatures (1700 and 1850 °C). The t- or c-phase volume fraction decreased as either the carbothermal reduction temperature or the porosity of the starting YSZ foam increased. Regarding the lattice parameters, the phase transformation from t-ZrO_2 to c-ZrC or c-ZrO_2 induced volume expansion, which would have an impact on the mechanical properties of the composite foam.

Figure 3 shows the microstructure of the 3YSZ template foam and ZrC/YSZ composite foam. Laminated cellular walls were well developed via the ice-templating process in 3YSZ template foams

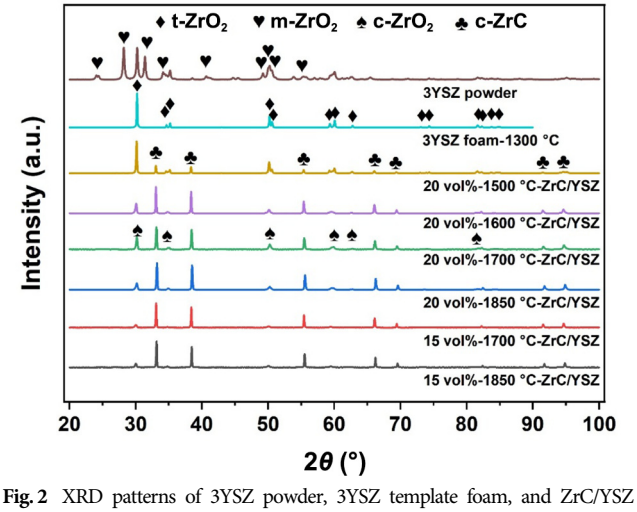

Fig. 2 XRD patterns of 3YSZ powder, 3YSZ template foam, and ZrC/YSZ composite foams.

(Figs. 3(a) and 3(d)) and kept in composite foams (Figs. 3(b), 3(c), and 3(e)–3(h)). The walls in the 3YSZ foams were almost fully dense. A layer of the c-ZrC phase was coated on the surface of the cellular walls, and particles of the c-ZrC phase were also unevenly distributed inside the cellular walls. Continuous t- or c-ZrO_2 phase was found in the matrix. The discovery that ZrC particles are observed inside cellular walls is unexpected but interesting since the microstructure of the 3YSZ cellular wall looks dense enough to block gases, such as CO, H_2O, H_2, and CO_2, released during pyrolysis of phenolic resin [25]. Furthermore, the porosity statistics and results from hypothesis testing in Fig. 3(i) show no significant difference in the ZrC/YSZ composite foam (probability values (P) of 0.18 and 0.32 for the 15 and 20 vol% ZrC/YSZ groups, respectively) but a significant difference (P: 0.0014) in the 3YSZ template foam group.

To confirm whether the particles inside the cellular wall were ZrC phase, EDS, and EPMA mappings were carried out to detect the distribution of C, Zr, O, and Y, as shown in Fig. 4. It is difficult to discriminate C segregation inside cellular walls from EDS element mappings, but it is clear to be seen in EPMA mappings. Moreover, Zr is also segregated, but Y and O are deficient in the location where C exists. In a previous study, the yttrium content did not exceed 2 wt% in ZrC, where the excess Y formed Y_2O_3 [26,27].

TEM images of the 20 vol%-1500 °C sample further show the formation of ZrC_xO_y, which is unevenly distributed around ZrO_2 grains in the cellular wall, as shown in Fig. 5. Here, the use of the formula ZrC_xO_y, where x and y are smaller than 1 and y is far less than x, to describe the ZrC phase product is because a small count of oxygen was quantified by EDS line scanning (Fig. 5(c)). Some ZrC_xO_y grains marked by white boxes in Fig. 5(a) were characterized via EDS mappings of C, Y, O, and Zr. Enlarged

Table 2 Phase compositions in powder derived using Rietveld refinement and phase volume fraction in foam multiplied by porosity

Sample ID	Porosity (%)	c-ZrC phase				t- or c-ZrO_2 phase					
		Space group	a (Å)	V_f (%) in powder	V_f (%) in foam	Space group	a (Å)	b (Å)	c (Å)	V_f (%) in powder	V_f (%) in foam
15 vol%-1700 °C	77.8 ± 2.3	$Fm\bar{3}m$	4.68661	76.9±0.6	17.1±1.8	$Fm\bar{3}m$	5.1536	—	—	23.1±0.3	5.1±0.5
15 vol%-1850 °C	79.2 ± 3.2	$Fm\bar{3}m$	4.67983	75.2±0.3	15.6±2.4	$Fm\bar{3}m$	5.15339	—	—	24.8±0.2	5.2±0.8
20 vol%-1500 °C	70.9 ± 3.7	$Fm\bar{3}m$	4.67923	16.9±0.5	4.9±0.6	$P42/nmc$	3.60368	3.60368	5.1653	83.1±2.9	24.2±3.2
20 vol%-1600 °C	72.1 ± 2.2	$Fm\bar{3}m$	4.68693	69.3±4.0	19.3±1.9	$P42/nmc$	3.62982	3.62982	5.16533	30.7±1.9	8.6±0.9
20 vol%-1700 °C	72.4 ± 3.3	$Fm\bar{3}$m	4.68737	57.4±2.4	15.8±2.0	$Fm\bar{3}m$	5.13785	—	—	42.6±3.1	11.8±1.6
20 vol%-1850 °C	73.8 ± 7.2	$Fm\bar{3}m$	4.68034	70.1±0.5	18.4±5.0	$Fm\bar{3}m$	5.14253	—	—	29.9±0.3	7.8±2.2

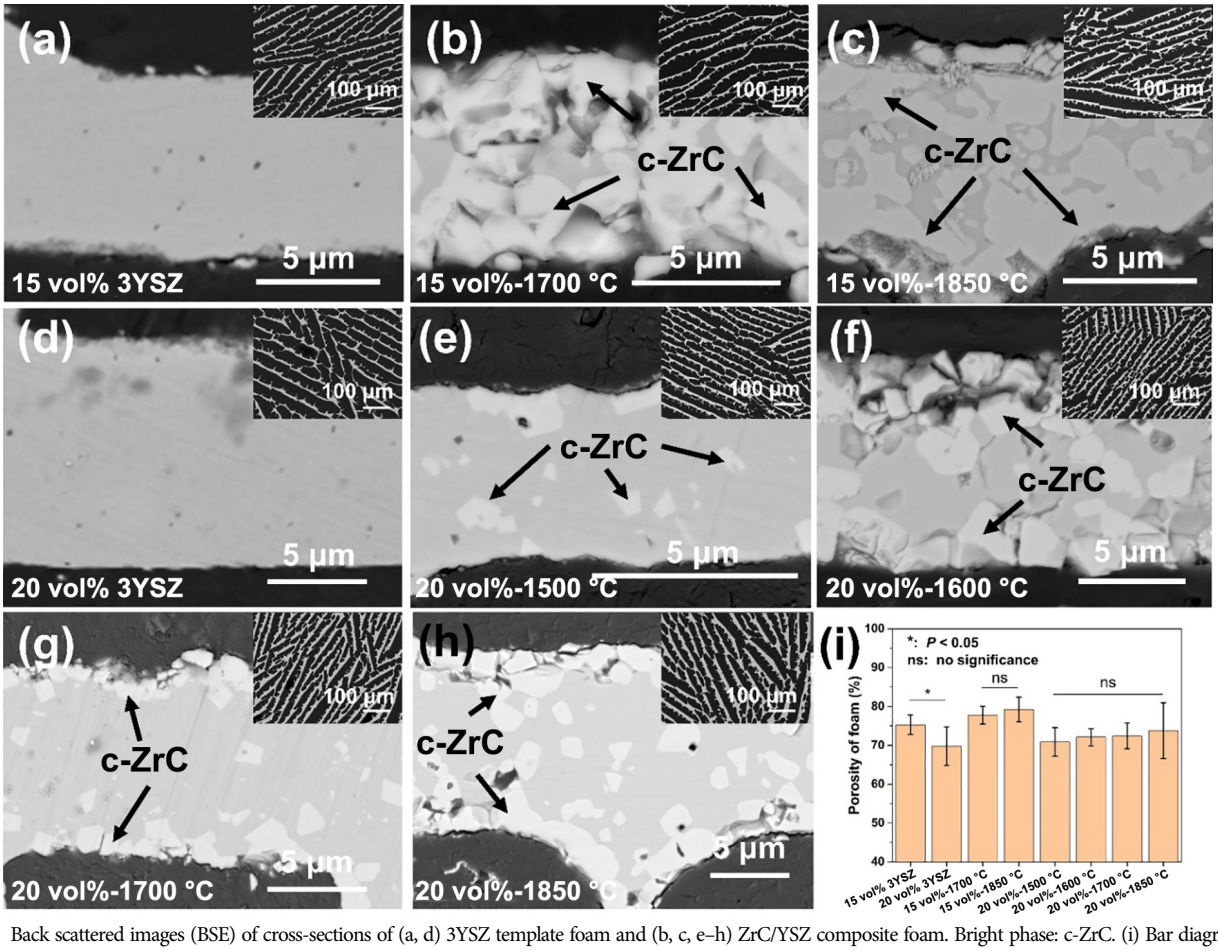

Fig. 3 Back scattered images (BSE) of cross-sections of (a, d) 3YSZ template foam and (b, c, e–h) ZrC/YSZ composite foam. Bright phase: c-ZrC. (i) Bar diagram of porosity. Inset images show laminated cellular walls.

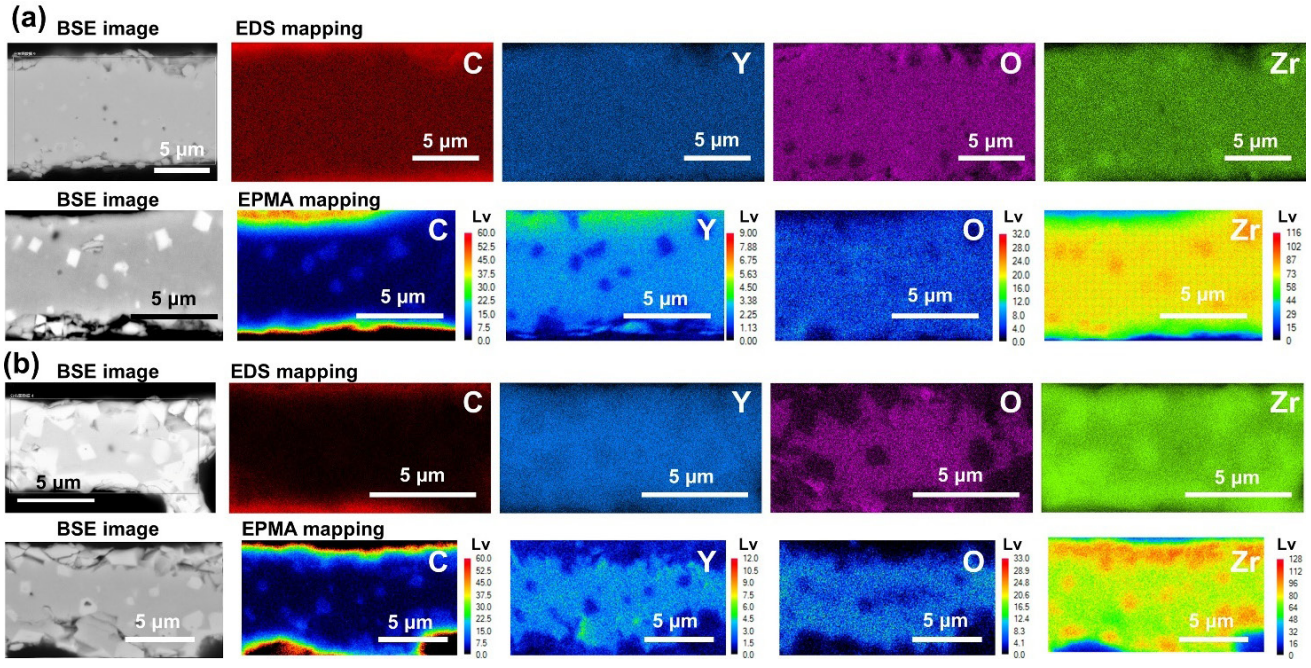

Fig. 4 BSE images and the corresponding EDS and EPMA mappings of (a) 15 vol%-1700 °C and (b) 20 vol%-1850 °C samples.

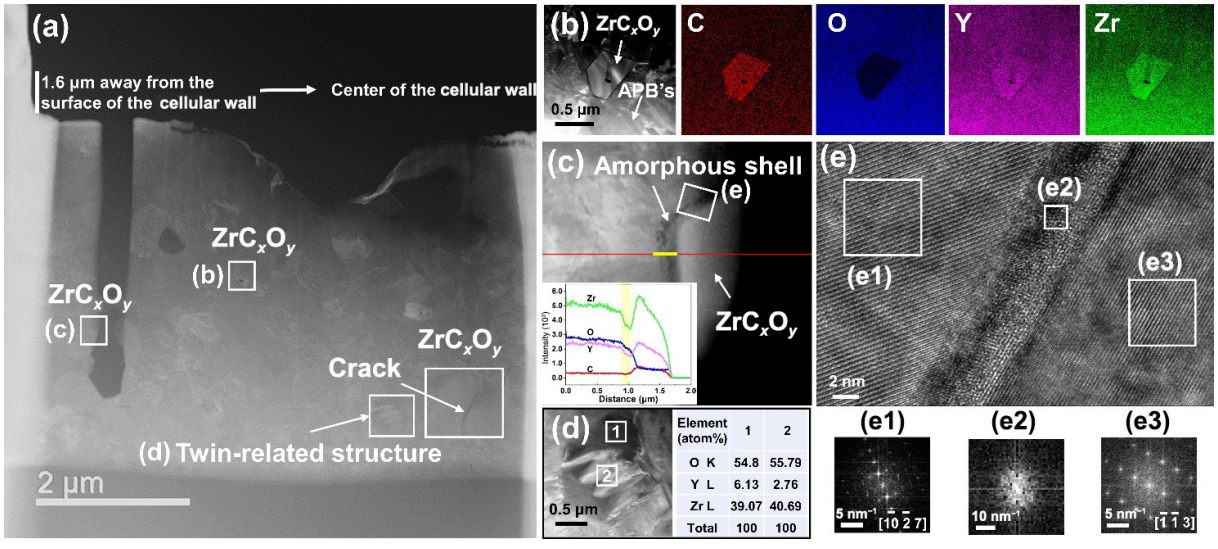

Fig. 5 TEM images of the 20 vol%-1500 °C sample prepared by focused ion beam (FIB). (a) Bright field image of cellular wall, (b) bright field image and its corresponding EDS mappings of C, O, Y, and Zr, and (c) EDS line scanning (position marked in red line) of ZrO_2 and ZrC_xO_y grains. (d) Twin-related structure in a ZrO_2 grain with Y concentration fluctuations. (e) High-resolution TEM image around amorphous shell and fast Fourier transforms of (e1) left box in Y-doped ZrO_2 grain, (e2) middle box in amorphous nanolayer, and (e3) right box in the ZrC_xO_y grain.

images and element distribution in Fig. 5(b) clearly show the segregation of C and the deficit of O. Twins and anti-phase domain boundaries (APBs) are also observed in ZrO_2 grains near ZrC_xO_y grains. An amorphous shell layer with a thickness of a few nanometers is clearly observed outside ZrC_xO_y grains, and Y and Zr lean in this layer, as shown in Figs. 5(c) and 5(e). Interestingly, the Y content in the twinning area (2.76 at%) was lower than that (6.13 at%) in the untransformed area. Chaim *et al.* [28] observed a 90° twin in ZrO_2-12 wt% Y_2O_3 after annealing at 1550 °C for 1 h and APB colonies of t-ZrO_2 formed by diffusional precipitation. The colony precipitates are actually stacked, twin-related plates sharing a {110} habit plane. This indicates that the *in situ* formation of ZrC_xO_y from ZrO_2 grains further impacts the Y^{3+} ion diffusion and phase structure of the YSZ matrix.

Figure 6 shows the grain morphology on the cellular wall surface of the composite and template foams. The surface of the ZrC/YSZ composite foam is not densely covered by the layer of ZrC grains since the space or interval between grains is exhibited in Figs. 6(a)–6(f), while ZrO_2 grains are close-packed on the surface of the 3YSZ template foam in Fig. 6(g). The size of the ZrC grains is ~1.9 μm, and the initial ZrO_2 grain size of the 3YSZ template foam is ~0.2 μm.

Figure 7 shows the longitudinal section of the ice-template 3YSZ foam. Several transverse cracks in dense cellular walls appear perpendicular to the main solidification direction. Such ice-lens type defects are also found in ice-templated alumina foam [29]. They potentially provide channels for phenolic resin infiltration and gases to diffuse.

Statistics on the cellular wall thickness and interlamellar spacing of the 3YSZ template foam and ZrC/YSZ composite foam by

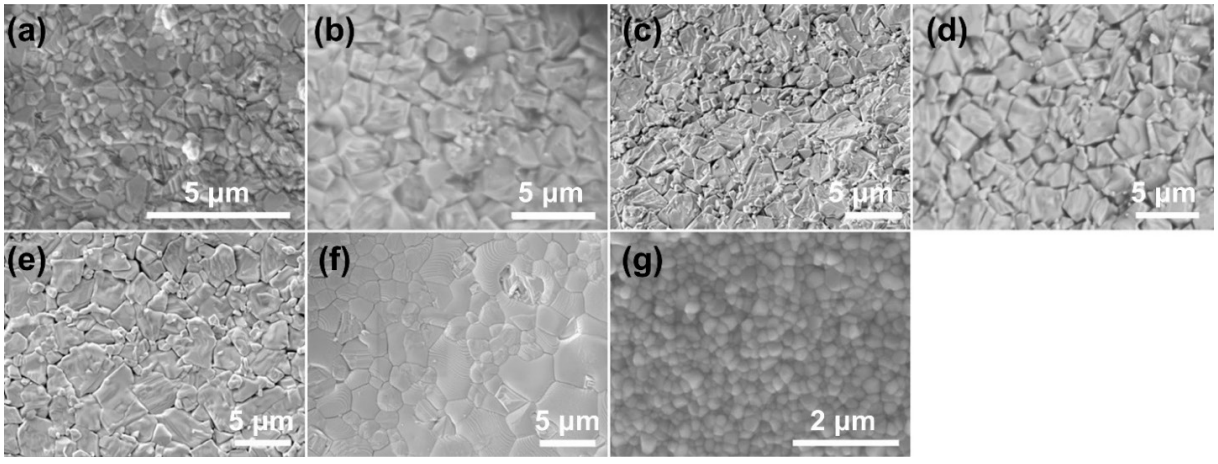

Fig. 6 Morphology on cellular wall surface of (a) 20 vol%-1500 °C, (b) 20 vol%-1600 °C, (c) 20 vol%-1700 °C, (d) 20 vol%-1850 °C, (e) 15 vol%-1700 °C, and (f) 15 vol%-1850 °C ZrC/YSZ composite foam, (g) 3YSZ template foam.

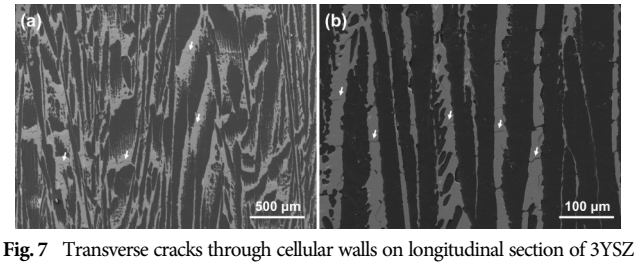

Fig. 7 Transverse cracks through cellular walls on longitudinal section of 3YSZ template foam (highlighted by white arrows).

ImageJ software are shown in Table 3. The ratio of wall thickness to interlamellar spacing was also calculated. Based on the extension of Gibson-Ashby theory, the out-of-plane compressive strength $\sigma$when loaded along the cell axis has a power-law relationship with cellular wall thickness (t_{cw}) to hole spacing l: $\sigma \propto C(t_{cw}/l)^m$, where C is a geometric constant, and m is set to be 1, 2, or 3 [30]. Therefore, the ratio of the mean wall thickness to the interlamellar spacing plays a key role in the mechanical behavior. For the 3YSZ template foam group, the ratio increases with solid loading. In both the 15 and 20 vol% ZrC/YSZ composite foam groups, the ratio increases with the carbo-thermal reduction temperature, except for the 20 vol%−1850 °C samples. The standard deviation of the wall thickness to interlamellar spacing ratio is relatively large because of the mathematical division operation and magnification of denominator errors.

Figures 8(a) and 8(b) show that most cracks in the composite foam after axial compression are transverse perpendicular to the direction of force application, and some cracks deflect in that direction. Intergranular fracture is in the majority on the cross section, and transgranular fracture is in the minority, as shown in Figs. 8(c) and 8(d). The failure of foam is caused by the buckling of cellular walls, which is the main reason for failure in ice-templated foam [19].

3.2 Compressive strength

The ZrC/YSZ composite foam has similar compressive behavior to the precursor of the 3YSZ template foam, exhibiting anisotropic

Table 3 Statistics on cellular wall thickness, interlamellar spacing, and ratio of 3YSZ template foam and ZrC/YSZ composite foam

Sample ID	Wall thickness (μm)	Interlamellar spacing (μm)	Wall thickness to interlamellar spacing
15 vol% 3YSZ	6.7±1.9	23.0±5.1	0.29±0.10
20 vol% 3YSZ	12.0±5.1	33.7±6.7	0.36±0.17
15 vol%-1700 °C	7.2±2.2	31.2±12.3	0.23±0.12
15 vol%-1850 °C	8.0±2.3	24.1±9.8	0.33±0.17
20 vol%-1500 °C	7.8±2.1	24.9±7.9	0.31±0.13
20 vol%-1600 °C	7.7±2.4	19.3±7.4	0.40±0.20
20 vol%-1700 °C	9.9±2.8	18.5±6.4	0.54±0.24
20 vol%-1850 °C	11.6±3.5	24.1±6.7	0.48±0.20

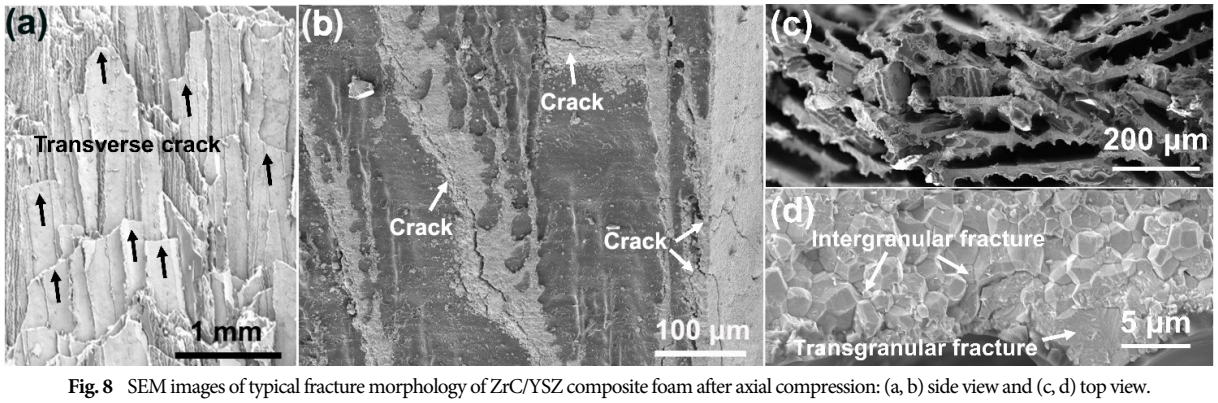

Fig. 8 SEM images of typical fracture morphology of ZrC/YSZ composite foam after axial compression: (a, b) side view and (c, d) top view.

characteristics, as shown in Fig. 9(a). Subject to axial loading, they show nonbrittle fracture. Foams are densified as radial loading increases. When the stress reaches the maximum value after the initial linear step (i.e., buckling strength), it then suddenly drops. Afterwards, the stress stabilizes to a constant value, and other failure events, such as progressive crushing of the struts, take place. This behavior agrees with a previous study on ice-templated YSZ foam [31]. The stress indicated by arrows was chosen as the compressive strength. Figure 9(b) shows the compressive strength statistics of the 3YSZ template foams and ZrC/YSZ composite foams under axial and radial loading. The axial compressive strengths of the 15 and 20 vol% 3YSZ template foams are 35.2±9.7 and 49.6±16.4 MPa, respectively. Considering their porosities of ~75.3% and 69.8%, these mechanical properties are reasonable because the compressive strength of 3YSZ micropillars with a porosity of 63% and random pore distribution is 147±22 MPa, as measured via uniaxial microcompression tests, and decreases with increasing porosity [32]. It is worth noting that the standard deviation of the axial compressive strength ranges from 3.0 to 22.6 MPa. Such a mechanical response agrees with ice-templated foams with water as the solvent [29]. The large error deviation of the axial compressive strength might be caused by the existence of macropores and cracks unevenly distributed in the cellular walls, as shown in Fig. S3 in the ESM.

Furthermore, the hypothesis testing results show a significant difference (P = 0.043) in the mean axial compressive strength between the 3YSZ template foams and no significance (P = 0.22) between the 15 vol% ZrC/YSZ composite foams. An ANOVA of 20 vol% ZrC/YSZ composite foams shows that the means are significantly different (P = 0.00013) between foams carbothermally reduced at different temperatures. Then, Tukey's test was carried out to evaluate the difference in pairs sequentially. Means of axial compressive strength that do not share a letter (A or B) show significant differences. The mean strength of the 20 vol%-1600 °C samples was not significantly different from that of the 20 vol%-1500 and 1700–1850 °C samples. Although the average strength at 1600 °C is significantly lower than that at 1500 °C, its variability renders the difference statistically insufficient to be deemed a significant decline. This marks the transition of strength from the high levels observed at 1500 °C to the lower levels encountered at 1700 °C.

Subject to radial loading, the average compressive strength of most foams ranges from 2.0 to 4.4 MPa, with a tiny difference and only one exception of 8.9 MPa for the 20 vol%-1850 °C ZrC/YSZ composite foam. However, the average axial compressive strength varies greatly depending on the solid loading and sintering temperature. This is further illustrated in Fig. 10 by considering the effects of the relative density, microstructure and phase composition of foams on the axial compressive strength.

In Fig. 10(a), the axial compressive strength increases as the relative density for the 3YSZ template foams and 15 and 20 vol% ZrC/YSZ composite foams increases. It also increases as the wall thickness to interlamellar spacing ratio in 3YSZ template foams, which are single phase materials. This is in good agreement with the Gibson-Ashby formula [30]. However, this rule does not apply to the ZrC/YSZ composite foams, as shown in Fig. 10(b). The axial compressive strength remains constant or decreases as the ratio increases. This indicates that the composition and content of phases in composite foams might contribute more to the axial compressive strength than their geometric structure. Figures 10(c) and 10(d) show the effects of the t-ZrO_2 and c-ZrC phase volume fractions on the compressive strength. It clearly reveals that the axial compressive strength increases with the content of t-ZrO_2 or c-ZrO_2, and the mechanical properties of the composite foam containing t-phase zirconia are superior to those containing c-phase zirconia, as shown in Fig. 10(c). A small volume fraction of c-ZrC in the composite foams, such as ~4.9 vol% for the 20 vol%-1500 °C samples, can strengthen the foam, but such a strengthening effect does not work when the ZrC content increases to more than 15 vol%, such as ~19.3 vol% for the 20 vol%–1600 °C samples. The tensile strength of t-ZrO_2 polycrystals (3YSZ) is reported to be ~700 MPa, markedly higher than that of c-ZrO_2 polycrystals (8YSZ, ~200 MPa) [33]. The t' phase decomposition into Y-poor t-ZrO_2 and Y-rich c-ZrO_2 during high-temperature annealing significantly decreases the bending strength of the air-plasma sprayed thermal barrier coating [34]. Therefore, t-ZrO_2 or c-ZrO_2 grains work as skeletal supports in the cellular walls of composite foams and make significant contributions to the compressive strength. A small amount of the c-ZrC phase (~5 vol%) can strengthen the t-ZrO_2 matrix. c-Phase ZrC with a content of more than 15 vol% and phase transformation from t to c give mechanical degradation. It is interesting that the axial compressive strength for the 20 vol%-1700 °C ZrC/YSZ samples has no significant difference from that of the 20 vol%-1600 °C samples, even though c-ZrO_2 was mainly found in the former and t-ZrO_2 was mainly found in the latter. It is noteworthy that under identical carbon thermal reduction conditions, the phase composition of the 15 vol% samples at 1500

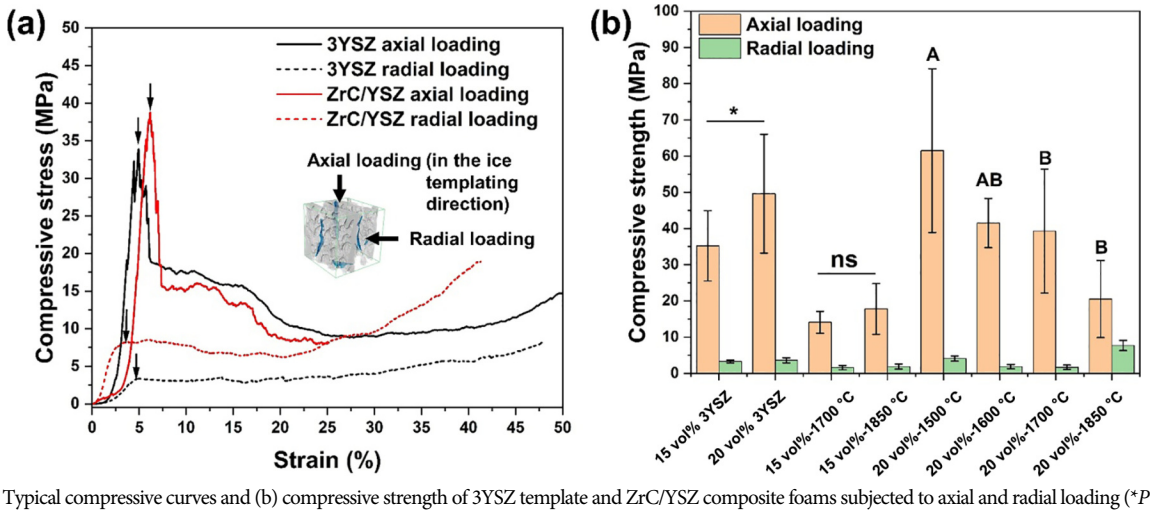

Fig. 9 (a) Typical compressive curves and (b) compressive strength of 3YSZ template and ZrC/YSZ composite foams subjected to axial and radial loading (*P < 0.05, ns: no significance, which means that do not share a letter are significantly different in 20 vol% ZrC/YSZ group).

清華大学出版社 Tsinghua University Press | SciOpen

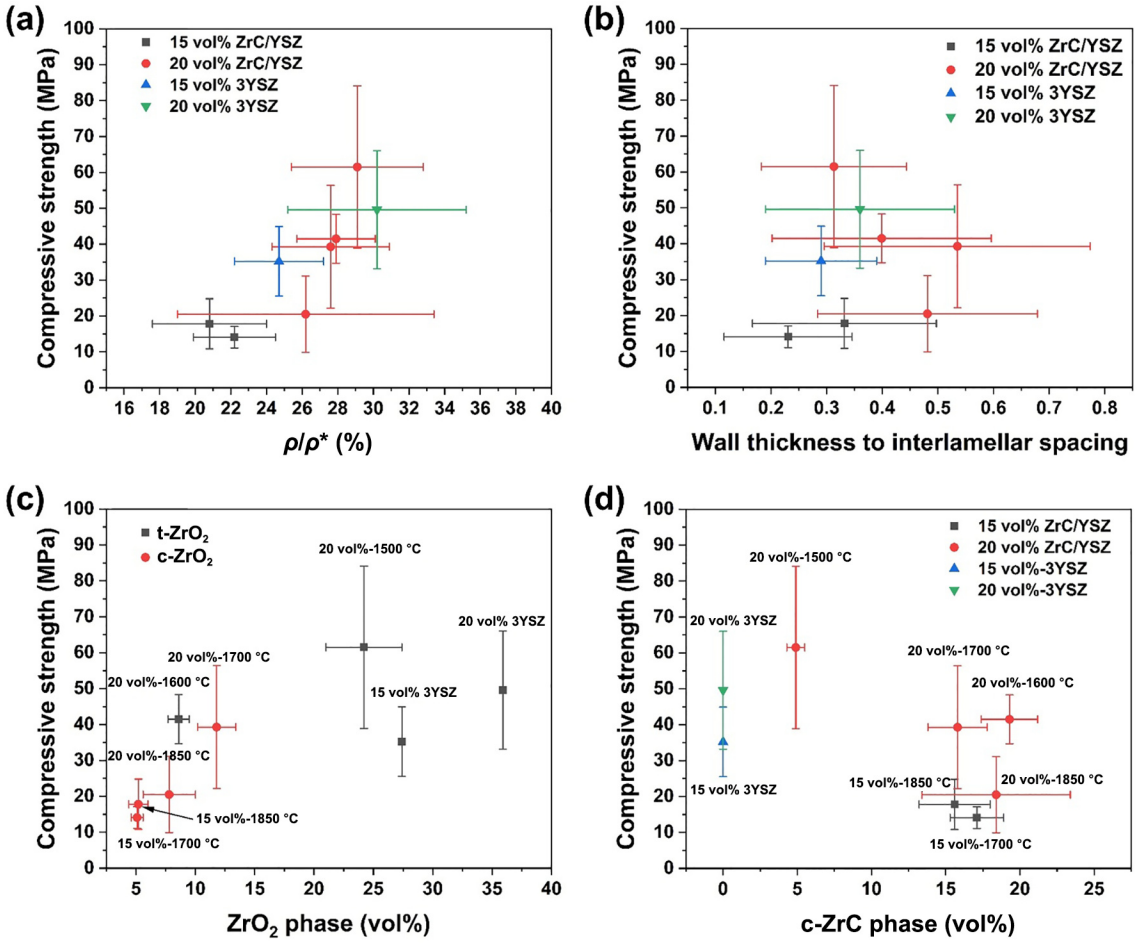

Fig. 10 Axial compressive strength of 3YSZ template and ZrC/YSZ composite foams as a function of (a) relative density, (b) wall thickness to interlamellar spacing, (c) ZrO_2 phase, and (d) c-ZrC phase volume fraction.

and 1600 °C is comparable to that of the 20 vol% samples at 1500 and 1600 °C, with similar mechanical property evolution. This is because the initial 15% and 20%-3YSZ template foams differ only in porosity and corresponding geometric structures.

3.3 *In situ* synthesis mechanism of ZrC/YSZ composite foam

Carbothermal reduction, which is used to industrially produce a large amount of powder, explains that the reduction of a metal oxide by carbon forms carbide together with the release of carbon monoxide as Eq. (1):

$$MO_x(s) + (1+x)C(s) = MC(s) + xCO(g) \quad (1)$$

Regarding ZrC, this transformation occurred via a solid-state reaction between zirconia and carbon. However, an intermediate phase, oxycarbide with a $ZrC_{0.71}O_{0.08}$ composition, was characterized by Kutsev *et al.* [35]. Maitre and Lefort [36] confirmed oxycarbide formation and deciphered a fine reaction mechanism by proposing two solid-gas reactions (Reactions (2) and (3)):

$$ZrO_2 + 0.84CO = ZrC_{0.84}O_{0.06} + 1.39O_2 \quad (2)$$

$$2.78C + 1.39O_2 = 2.78CO \quad (3)$$

More recently, another partial reaction, corresponding to a solid-gas reaction (Reaction (4)):

$$ZrO_2(s) + CO(g) = ZrO(g) + CO_2(g) \quad (4)$$

was proposed to explain the oxycarbide nucleation located within the carbon black and covered by an amorphous layer [37]. The covering layer was formed as a consequence of a cocondensation phenomenon of ZrO (g) and CO (g) gaseous species through a gas-gas reaction (Reaction (5)):

$$ZrO(g) + 2.71CO(g) = ZrC_{0.89}O_{0.07}\square_{0.04}(s) + 1.82CO_2(g) \quad (5)$$

Previous studies point out that the diffusion of gas species plays an important role in intermediate ZrC_xO_y nucleation and growth. Interlayer spacing between YSZ and pyrocarbon layers was observed in the precursor of the ZrC/YSZ composite foam after high-temperature pyrolysis of phenolic resin, as shown in the mounting resin area of Fig. 11. Gas can easily diffuse through open channels between the pyrocarbon layer and YSZ layer. However, ZrC grains formed inside the YSZ cellular wall are first observed and are quite uncommon because the diffusion of carbon or carbon monoxide in dense YSZ is quite limited [27,38]. Moreover, there is no pyrocarbon found in the YSZ cellular walls of the precursor foam after pyrolysis of phenolic resin by Raman spectroscopy, as shown in Figs. 11(b) and 11(c). Peaks at 150, 262, 323, 466, 605, and 644 cm^{-1} were characteristic of YSZ. Typical Raman bands on polycrystalline ZrC at 210, 280, 520, and 615 cm^{-1} [39] were not observed in the cellular wall. In the pyrocarbon zone, peaks at 1334 and 1588 cm^{-1} are mainly identified, characteristic of graphite. It is interesting that other

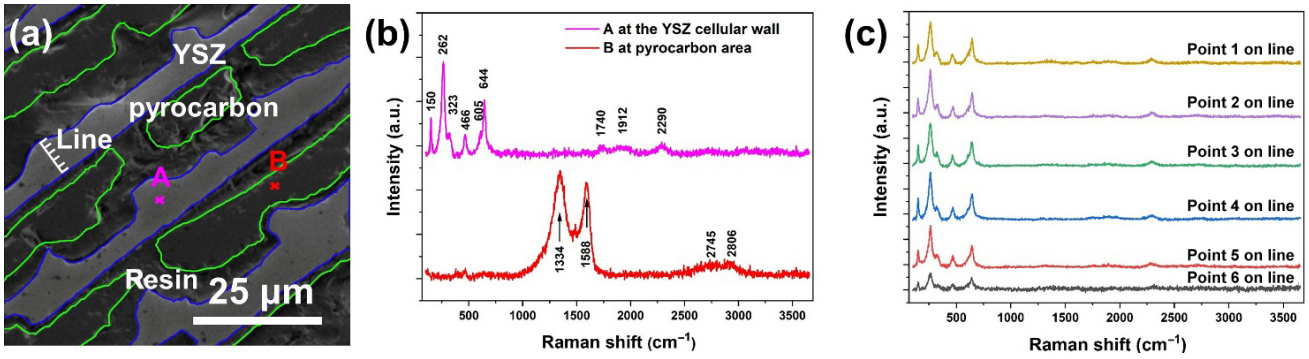

Fig. 11 Precursor of ZrC/YSZ composite foam after phenolic resin pyrolysis at 1100 °C: (a) second electron image on cross-section (outline of pyrocarbon is represented by green line and YSZ by blue line, mounting resin was filled in between them). (b) Raman shift spectra of YSZ and pyrocarbon. (c) Raman line scan.

peaks, such as 1740, 1912, and 2290 cm^{-1}, were found in the line-scan Raman spectrum of the cellular wall. Other allotropes of carbon, such as carbyne (1050 cm^{-1} for C–C, 2175 cm^{-1} for C≡C) [40] and graphyne (2241 cm^{-1}) [41], were speculated. A nitrile functional group (2100–2300 cm^{-1} for C≡N) [42] was also considered. However, none of the carbon and its allotropes were characterized on ZrO_2 grain boundaries by TEM images of the cellular wall cut from the precursor foam. ZrC_xO_y grains were also not observed. Hence, graphite and other carbon allotropes scarcely invade the YSZ cellular wall before the carbothermal reduction reaction. In other words, nucleation and growth of ZrC_xO_y grains start in the carbon-thermal reduction process at elevated temperatures (> 1100 °C). The nucleation of ZrC_xO_y around ZrO_2 grains is closely related to the diffusion and reaction of CO and ZrO gases. Preexisting cracks and open channels in the YSZ template foam likely provide pathways for gas diffusion and reaction.

The formation of ZrC_xO_y grains usually involves two steps: the nucleation and growth of the oxycarbide phase and the maturation of oxycarbide. David *et al.* [37] found that the heterogeneous nucleation of oxycarbide is strictly located with carbon. However, little graphite after pyrolysis of phenolic resin was left on the surface of the YSZ cellular wall, and little carbon was present inside. This indicated that carbon deposition on the surface of ZrO_2 grains occurred before oxycarbide nucleation. In the following CO, the inverse Boudouard reaction $2CO\,(g) \rightarrow C\,(s) + CO_2(g)$ could promote a carbon layer of disordered nanocrystalline graphite covering the respective oxide at elevated temperatures above ~1023 K. Kogler *et al.* [43] proved that C–O bond scission at surface vacancies and/or defects on YSZ, Y_2O_3, and ZrO_2 substrates was induced, leaving a highly distorted graphitic carbon layer. The graphite layer tended to gradually grow localized without coalescence or percolation. A vacancy-mediated pathway provides graphite islands or clusters deposited on the ZrO_2 grain surface, where the zirconium oxycarbide nucleates. A condensation phenomenon arises around graphite clusters through the gas-gas reaction between CO (g) and ZrO (g) in Reaction (5). An amorphous layer between parent ZrO_2 grains and product ZrC_xO_y grains forms and migrates with the destabilization of zirconia.

The destabilization of zirconia via a zipper-type mechanism is associated with Wadsley-type defects in a CO-reduced atmosphere, releasing ZrO gas [43]. Because the Y^{3+} ion is more stable and its activation enthalpy of bulk diffusion (4.2 eV) is slightly smaller than that of zirconium in zirconia (4.5 eV) [44], affluent yttria addition in parent ZrO_2 grains is reserved. Y^{3+} ions enrich or segregate at the grain boundaries by electrostatic attraction, and oxygen vacancies rapidly increase to balance the charge of Y^{3+} ions. Y^{3+} ions accompanied by oxygen vacancies are more energetically favorable to segregate at grain boundaries, as their segregation can effectively reduce strains [45]. However, considerable lattice strain is proposed to develop from compositional differences because grain boundaries migrate from Y-rich grains through Y-poor grains, leaving the Y^{3+} concentration difference behind. The redistribution of Y^{3+} ions in neighboring zirconia grains via lattice diffusion at elevated temperature induces lattice distortion. During annealing at 1700–1850 °C, the new equilibrium of Y^{3+} is associated with the t to Y-rich c phase transformation, which agrees well with a previous study demonstrating that the diffusion of Y^{3+} in zirconia caused the t to c phase transformation [46]. However, after 1500–1600 °C annealing for 2 h, APBs precipitated in neighboring ZrO_2 grains formed by a diffusion-controlled pro-eutectoid precipitation reaction, and deformed twins in the Y-poor area were also observed near the Y-rich area. Clearly, APB and twins are a means of reducing the strain energy. The remaining coherency strain in such a colony microstructure is confined to a small region adjacent to the precipitate/matrix interface. As Katchaturyan predicted [47], an adaptive martensite formation is expected as an elastically constrained phase when the scale of structural heterogeneities induced by the crystal-strain accommodation is reduced to the microscopic scale commensurate with the twin-plane interplanar distance.

Notably, although XRD patterns (Fig. 2) of all these ZrC/YSZ composite foams show virtually no graphite content, SEM images (Fig. S4 in the ESM) reveal trace amounts of residual pyrocarbon on the cellular wall surfaces. This indicates that the content of residual pyrocarbon is limited. The system coupled reactions (Eqs. (3) and (4)) involving the destabilization of the two parent solid phases (ZrO_2 and graphite) are broken due to the shortage of pyrocarbon and CO. The maturity of the intermediate oxycarbide is also limited, as the amorphous shell of the ZrC_xO_y grain is observed in the TEM images (Fig. 5(b)).

In summary, an *in situ* synthesis mechanism of ZrC grains within 3YSZ cellular walls is proposed, as shown in Fig. 12. It involves three steps: (1) deposition of disordered graphite, (2) nucleation of oxycarbide, and (3) growth and of oxycarbide. During high-temperature annealing, pyrocarbon is first oxidized to create carbon monoxide and a reduced atmosphere at the very beginning. Decomposition of the parent zirconia phase by carbon monoxide releases ZrO and carbon dioxide gases. An inverse Boudouard reaction occurs on the surface of the zirconia matrix, especially at grain boundaries, leaving disordered graphite clusters. In the second step, nucleation of ZrC_xO_y occurs via condensation of ZrO (g) and CO (g) around the graphite cluster. There is an amorphous shell outside the core of ZrC_xO_y. Y^{3+} ions are enriched near grain boundaries and diffuse via grain boundary net or lattice diffusion. In the third step, the nucleate of ZrC_xO_y grows and

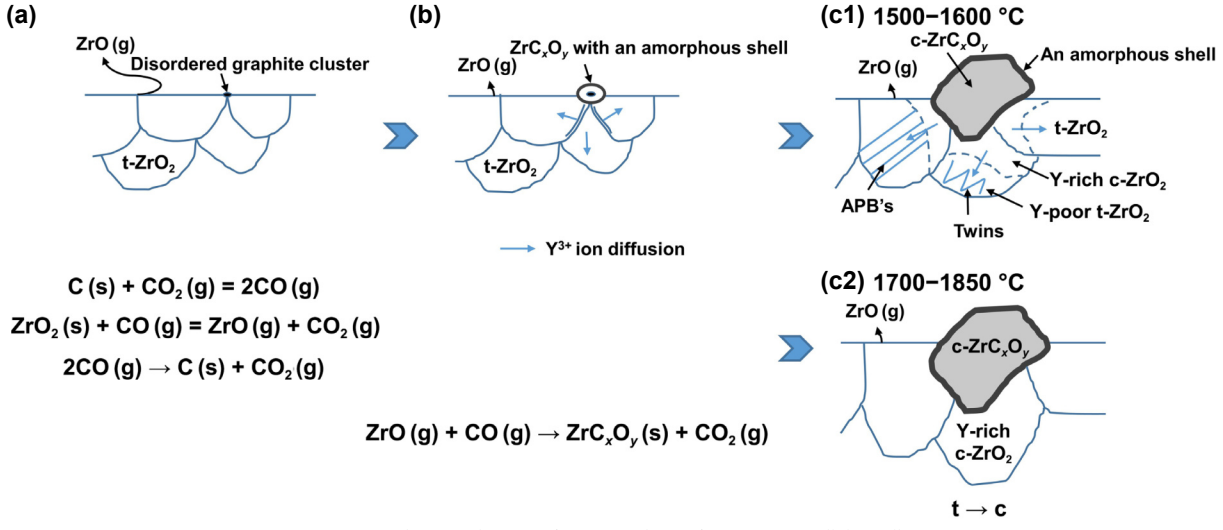

Fig. 12 Schematic diagram of *in situ* synthesis of ZrC in 3YSZ cellular wall.

polygonizes as the amorphous shell migrates toward the zirconia matrix, where t → c phase transformations reduce the strain energy caused by lattice distortion from yttria enrichment. At relatively low temperatures, e.g., 1500–1600 °C, APB and twin structures precipitate in Y-poor areas to eliminate lattice mismatch. The c phase, fully stabilized zirconia with yttria, is dominant at higher carbothermal reduction temperatures (1700–1850 °C).

3.4 Inherent limitation of this method on mechanical properties

A series of anisotropic high-strength ZrC/YSZ composite foams are successfully prepared by introducing ice-templated YSZ foam as a reactive template. The compressive strength of ZrC/YSZ preserved the anisotropic characteristics of the YSZ template foam. The results show that the phase type and content of residual YSZ grains mainly contribute to the strength over the relative density and geometric structure of porous ceramics. The mechanical properties of the ZrC/YSZ composite foam might be inherently limited by the adaptive phase transformation of the YSZ strut, which is strongly dependent on the preparation temperature.

It is expected to obtain more c-ZrC phase in the composite foam by increasing the carbothermal reduction temperature above 1600 °C. However, the compressive strength of the ZrC/YSZ composite foam prepared at 1700 and 1850 °C decreases due to the deficiency of t-ZrO_2 grains. At that high temperature, t-ZrO_2 grains not only decompose to supply the formation of ZrC_xO_y grains but also transform into the c-ZrO_2 phase. On the one hand, the Y-rich c-ZrO_2 phase has a lower strength than the Y-poor t-ZrO_2 phase [33]. The adaptive phase transformation of t to c introduces lattice distortion nearby, causing some compatible deformation, such as twins and APB in the Y-poor area, and some uncoordinated deformation, such as microcracks. On the other hand, the new c-ZrC phase is poorer in strength and fracture toughness than ZrO_2 at room temperature [20]. Microcracks caused by localized lattice distortion of nearby zirconia grains can pass through ZrC_xO_y grains. Hence, it is recommended to synthesize high-strength ZrC/YSZ porous ceramics *in situ* at temperatures not exceeding 1600 °C.

4 Conclusions

This study aimed to prepare high-strength ZrC-based foam with high porosity. We developed an *in situ* synthesis of a ZrC/YSZ composite foam approach, in which ice-templated 3YSZ foam was carbothermally reduced at temperatures above 1500 °C by using pyrocarbon from phenolic resin as a carbon source. It was first observed that ZrC grains nucleated and grew nearby YSZ grains, and a schematic of their synthesis is illustrated. The diffusion of Y^{3+} ions in the parent ZrO_2 phase induces an adaptive phase transformation (t to c), which is dependent on the annealing temperature, to reduce the strain energy from lattice distortion. Although phase transformation degrades the strength of the ZrC/YSZ composite foam, YSZ struts are expected to provide excellent support. The axial compressive strength of the composite foam, which exhibited porosities of 70.9%–77.8%, ranged from 20.5 to 61.5 MPa. These results suggest that high-strength ZrC/YSZ composite foam should be prepared at temperatures not exceeding 1600 °C. Future work could focus on investigating the effect of the initial Y doping content on the *in situ* carbothermal reduction of the YSZ matrix to ZrC and the thermal stability and performance of composite foams at elevated temperature.

Acknowledgements

This research is supported by the opening project (No. 6142912200202) from the National Key Laboratory of Science and Technology for National Defense on High-Strength Structural Materials (Central South University). This research was also supported by the National Natural Science Foundation of China (Nos. 52373292 and 51902197) and the Fundamental Research Funds for the Central Universities (Nos. 24X010301285 and 21X010301700).

Availability of data and materials

The data that support the findings of this study are available from the corresponding author upon reasonable request.

Competing interests

The authors have no competing interests to declare that are relevant to the content of this article.

Electronic Supplementary Material

Supplementary material is available in the online version of this article at https://doi.org/10.26599/JAC.2026.9221247.

References

[1] Paul A, Venugopal S, Binner J, *et al.* UHTC composites for hypersonic applications. *Am Ceram Soc Bull* 2012, **91**: 22–8.

[2] Ifti HS, Hermann T, Ewenz Rocher M, *et al.* Laminar transpiration cooling experiments in hypersonic flow. *Exp Fluids* 2022, **63**: 102.
[3] Information on https://findanexpert.unimelb.edu.au/project/18949-multi-scale-porous-ultra-high-temperature-ceramics.
[4] Chen H, Xiang HM, Dai FZ, *et al.* Low thermal conductivity and high porosity ZrC and HfC ceramics prepared by *in-situ* reduction reaction/partial sintering method for ultrahigh temperature applications. *J Mater Sci Technol* 2019, **35**: 2778–2784.
[5] Chen H, Xiang HM, Dai FZ, *et al.* High porosity and low thermal conductivity high entropy $(Zr_{0.2}Hf_{0.2}Ti_{0.2}Nb_{0.2}Ta_{0.2})C$. *J Mater Sci Technol* 2019, **35**: 1700–1705.
[6] Yan NN, Fu QG, Zhang YY, *et al.* Preparation of pore-controllable zirconium carbide ceramics with tunable mechanical strength, thermal conductivity and sound absorption coefficient. *Ceram Int* 2020, **46**: 19609–19616.
[7] Li F, Huang X. Preparation of highly porous ZrB_2/ZrC/SiC composite monoliths using liquid precursors via direct drying process. *J Eur Ceram Soc* 2018, **38**: 1103–1111.
[8] Li F, Huang X, Liu JX, *et al.* Sol-gel derived porous ultra-high temperature ceramics. *J Adv Ceram* 2020, **9**: 332.
[9] Li F, Kang Z, Huang X, *et al.* Preparation of zirconium carbide foam by direct foaming method. *J Eur Ceram Soc* 2014, **34**: 3513–3520.
[10] Li CY, Gao RN, Ouyang HB, *et al.* Hierarchical porous $(Ta_{0.2}Nb_{0.2}Ti_{0.2}Zr_{0.2}Hf_{0.2})C$ high-entropy ceramics prepared by a self-foaming method for thermal insulation. *J Adv Ceram* 2024, **13**: 956–966.
[11] Jiang JM, Wang S, Li W, *et al.* Fabrication and characterization of ZrC foam by melt infiltration. *J Alloys Compd* 2017, **695**: 2295–2300.
[12] Zhao K, Ye F, Cheng LF, *et al.* Formation of ultra-high temperature ceramic hollow microspheres as promising lightweight thermal insulation materials via a molten salt-assisted template method. *ACS Appl Mater Inter* 2021, **13**: 37388–37397.
[13] Ohji T, Fukushima M. Macro-porous ceramics: Processing and properties. *Int Mater Rev* 2012, **57**: 115–131.
[14] Okada K, Isobe T, Katsumata KI, *et al.* Porous ceramics mimicking nature-preparation and properties of microstructures with unidirectionally oriented pores. *Sci Technol Adv Mater* 2011, **12**: 064701.
[15] Landi E, Sciti D, Melandri C, *et al.* Ice templating of ZrB_2 porous architectures. *J Eur Ceram Soc* 2013, **33**: 1599–1607.
[16] Rambo CR, Cao J, Rusina O, *et al.* Manufacturing of biomorphic (Si,Ti,Zr)-carbide ceramics by sol–gel processing. *Carbon* 2005, **43**: 1174–1183.
[17] Dominguez-Rodriguez A, Heuer AH. Precipitation toughening and precipitation hardening in Y_2O_3-stabilized ZrO_2 crystals. *Nato Adv Sci I E-app* 1989, **3**: 761–776.
[18] Hu LF, Wang CG. Effect of sintering temperature on compressive strength of porous yttria-stabilized zirconia ceramics. *Ceram Int* 2010, **36**: 1697–1701.
[19] Zou JZ, Xiong HW, Huang YJ, *et al.* Fracture mode and compressive strength of ice-templated porous zirconia. *Ceram Int* 2021, **47**: 17373–17382.
[20] Min-Haga E, Scott WD. Sintering and mechanical properties of ZrC-ZrO_2 composites. *J Mater Sci* 1988, **23**: 2865–2870.
[21] Li F, Bao WC, Ni DW, *et al.* A thermoset hybrid sol for the syntheses of zirconium carbide–silicon carbide foam via replica method. *J Porous Mat* 2019, **26**: 409–417.
[22] Li F, Wang XG, Huang X, *et al.* Preparation of ZrC/SiC porous self-supporting monoliths via sol-gel process using polyethylene glycol as phase separation inducer. *J Eur Ceram Soc* 2018, **38**: 4806–4813.
[23] Li XW, Fan XH, Ni N, *et al.* Continuous alumina fiber-reinforced yttria-stabilized zirconia composites with high density and toughness. *J Eur Ceram Soc* 2020, **40**: 1539–1548.
[24] Fan XH, Ni N, Wang X, *et al.* Mechanically isotropic alumina prepared by spark plasma sintering: The role of pyrolytic carbon and multilayer graphene. *J Eur Ceram Soc* 2021, **41**: 4242–4251.
[25] Trick KA, Saliba TE. Mechanisms of the pyrolysis of phenolic resin in a carbon/phenolic composite. *Carbon* 1995, **33**: 1509–1515.
[26] Samsonov GV, Lavrenko VA, Neshpor VS, *et al.* Reaction of hydrogen atoms with the surface of yttrium-containing zirconium carbide. *Sov Powder Metall+* 1975, **14**: 751–752.
[27] Sondhi A. Investigations in the mechanism of carbothermal reduction of yttria stabilized zirconia for ultra-high temperature ceramics application and its influence on yttria contained in it. Ph.D. Thesis. Denton (USA): University of North Texas Libraries, 2014.
[28] Chaim R, Rühle M, Heuer AH. Microstructural evolution in a ZrO_2Wt% Y_2O_3 Ceramic. *J Am Ceram Soc* 1985, **68**: 427–431.
[29] Deville S, Meille S, Seuba J. A meta-analysis of the mechanical properties of ice-templated ceramics and metals. *Sci Technol Adv Mater* 2015, **16**: 043501.
[30] Gibson LJ, Ashby MF. Cellular solids. vol. 15. 2nd ed. 2001.
[31] Seuba J, Deville S, Guizard C, *et al.* The effect of wall thickness distribution on mechanical reliability and strength in unidirectional porous ceramics. *Sci Technol Adv Mater* 2016, **17**: 128–135.
[32] Abaza A, Meille S, Nakajo A, *et al.* Fracture of porous ceramics: Application to the mechanical degradation of solid oxide cell during redox cycling. *ECS Trans* 2021, **103**: 1151–1163.
[33] Kondoh J, Shiota H, Kawachi K, *et al.* Yttria concentration dependence of tensile strength in yttria-stabilized zirconia. *J Alloys Compd* 2004, **365**: 253–258.
[34] Ren XR, Pan W. Mechanical properties of high-temperature-degraded yttria-stabilized zirconia. *Acta Mater* 2014, **69**: 397–406.
[35] Kutsev VS, Epelbaum BF, Ormont VA. Equilibrium of the ZrO_2–C system at high temperatures. *Dokl Akad Nauk Sssr+* 1955, **104**: 567.
[36] Maitre A, Lefort P. Solid state reaction of zirconia with carbon. *Solid State Ionics* 1997, **104**: 109–122.
[37] David J, Trolliard G, Gendre M, *et al.* TEM study of the reaction mechanisms involved in the carbothermal reduction of zirconia. *J Eur Ceram Soc* 2013, **33**: 165–179.
[38] Vykhodets VB, Kurennykh TE, Kesarev AG, *et al.* Diffusion of insoluble carbon in zirconium oxides. *Jetp Lett+* 2011, **93**: 5–9.
[39] Pellegrino S, Trocellier P, Thomé L, *et al.* Raman investigation of ion irradiated TiC and ZrC. *Nucl Instrum Meth B* 2019, **454**: 61–67.
[40] Pan BT, Xiao J, Li JL, *et al.* Carbyne with finite length: The one-dimensional sp carbon. *Sci Adv* 2015, **1**: 1500857.
[41] Thapliyal V, Alabdulkarim ME, Whelan DR, *et al.* A concise review of the Raman spectra of carbon allotropes. *Diam Relat Mater* 2022, **127**: 109180.
[42] Mojica EE, Abbas N, Wyan LO, *et al.* Solvent sensitivity of the–C≡N group: A Raman spectroscopic study. *Raman Spectroscopy in the Undergraduate Curriculum* 2018: 181–197.
[43] Kogler M, Köck EM, Klötzer B, *et al.* High-temperature carbon deposition on oxide surfaces by CO disproportionation. *J Phys Chem C* 2016, **120**: 1795–1807.
[44] Kilo M, Taylor MA, Argirusis C, *et al.* Cation self-diffusion of Ca44, Y88, and Zr96 in single-crystalline calcia- and yttria-doped zirconia. *J Appl Phys* 2003, **94**: 7547–7552.
[45] Yoshiya M, Oyama T. Impurity and vacancy segregation at symmetric tilt grain boundaries in Y_2O_3-doped ZrO_2. *J Mater Sci* 2011, **46**: 4176–4190.
[46] Xu YG, Huang ZH, Liu YG, *et al.* Influence of yttria addition on the phase transformations of zirconia from zircon ore by carbothermal reduction process. *Solid State Sci* 2012, **14**: 730–734.
[47] Khachaturyan A, Shapiro S, Semenovskaya S. Adaptive phase formation in martensitic transformation. *Phys Rev B* 1991, **43**: 10832–10843.